Self-assembly of magnetic nanoclusters in diamond-like carbon by diffusion processes enhanced by collision cascades

P. Gupta, G. V. M. Williams, R. Hübner, S. Vajandar, T. Osipowicz, K-H. Heinig, H-W. Becker, and A. Markwitz

Citation: Appl. Phys. Lett. **110**, 141901 (2017); doi: 10.1063/1.4979523
View online: http://dx.doi.org/10.1063/1.4979523
View Table of Contents: http://aip.scitation.org/toc/apl/110/14
Published by the American Institute of Physics

Self-assembly of magnetic nanoclusters in diamond-like carbon by diffusion processes enhanced by collision cascades

P. Gupta,[1,2] G. V. M. Williams,[2] R. Hübner,[3] S. Vajandar,[4] T. Osipowicz,[4] K-H. Heinig,[3] H-W. Becker,[5] and A. Markwitz[1,2]

[1]*Department of Materials and Air, National Isotope Centre, GNS Science, PO Box 31-312, Lower Hutt 5010, New Zealand*
[2]*The MacDiarmid Institute for Advanced Materials and Nanotechnology, School of Chemical and Physical Sciences, Victoria University of Wellington, PO Box 600, Wellington 6040, New Zealand*
[3]*Institute of Ion Beam Physics and Materials Research, Helmholtz-Zentrum Dresden-Rossendorf, PO Box 510119, Dresden 01314, Germany*
[4]*The Centre for Ion Beam Applications, Department of Physics, National University of Singapore, Singapore 117542*
[5]*RUBION, Ruhr-University Bochum, Bochum 44780, Germany*

(Received 11 December 2016; accepted 17 March 2017; published online 3 April 2017)

Mono-energetic cobalt implantation into hydrogenated diamond-like carbon at room temperature results in a bimodal distribution of implanted atoms without any thermal treatment. The ~100 nm thin films were synthesised by mass selective ion beam deposition. The films were implanted with cobalt at an energy of 30 keV and an ion current density of ~5 μA cm^{-2}. Simulations suggest the implantation profile to be single Gaussian with a projected range of ~37 nm. High resolution Rutherford backscattering measurements reveal that a bimodal distribution evolves from a single near-Gaussian distribution as the fluence increases from 1.2 to 7×10^{16} cm^{-2}. Cross-sectional transmission electron microscopy further reveals that the implanted atoms cluster into nanoparticles. At high implantation doses, the nanoparticles assemble primarily in two bands: one near the surface with nanoparticle diameters of up to 5 nm and the other beyond the projected range with ~2 nm nanoparticles. The bimodal distribution along with the nanoparticle formation is explained with diffusion enhanced by energy deposited during collision cascades, relaxation of thermal spikes, and defects formed during ion implantation. This unique distribution of magnetic nanoparticles with the bimodal size and range is of significant interest to magnetic semiconductor and sensor applications. *Published by AIP Publishing*. [http://dx.doi.org/10.1063/1.4979523]

Doping of semiconductors with magnetic ions is being actively pursued for two major applications: magnetic semiconductors for spintronics and high magnetoresistances for magnetic sensing. Manganese doped GaAs, for example, is known to be a low temperature dilute magnetic semiconductor.[1] Room temperature ferromagnetism is observed when magnetic ions, such as e.g., Co, are doped into semiconductors such as TiO_2, but there are uncertainties concerning the origin of the magnetic order.[2] Some studies have suggested that it can arise from magnetic nanoparticles.[3,4] The appearance of nanoparticles can be advantageous for some applications because they can lead to high magnetoresistances[5] that can be quasilinear at high magnetic fields.[5] Different methods have been used to create magnetic semiconductors such as atomic layer deposition,[6] chemical vapour deposition,[7] and molecular beam epitaxy.[8] Apart from the complex processing involved, the choice of material requires these methods to provide an accurate control over their crystalline structure without compromising on delivering the required charge carrier concentration.

Ion implantation offers a precise control over dopant concentration, range, and distribution. It is inherently a non-equilibrium process known to overcome the solubility limits in materials.[9] Recent reports on ion implanted nanocomposites show several useful magnetic and transport properties.[2,10–12] However, the defects accumulated during implantation can upset the compatibility of the material in device applications. We chose hydrogenated diamond-like carbon (DLC) as our base material. Unlike compound semiconductors, DLC fabrication can be relatively simple and cost-effective.[13–15] Ion implantation into DLC offers an additional unique opportunity to increase the compatibility of DLC for device electronics, for example, by enhancing its electrical conductivity.[16] This is achieved by rehybridisation of carbon from sp^3 to sp^2 bonding and by controlling the size of sp^2 carbon clusters during implantation.[16]

Magnetic doping into DLC has been attempted in the past to obtain high magnetoresistances and intrinsic magnetism. For example, Santana *et al.* reported a negative room temperature magnetoresistance after chromium doping of DLC.[17,18] Interestingly, the magnetic order did not persist at room temperature. Paul *et al.* on the other hand doped DLC with nickel to obtain room temperature ferromagnetism,[19] yet the magnetic order is not intrinsic in nature as no chemical interaction between nickel nanoparticles and DLC was detected. In our previous work, we reported room temperature magnetic order in Co implanted DLC with a range of Curie temperatures.[20] We theorised that this could arise from an inhomogeneous distribution of magnetic atoms in the DLC matrix.[20]

In this letter, we present the results from transmission electron microscopy (TEM) and high resolution RBS

measurements of low-energy Co implanted DLC films. We find that magnetic nanoparticles form during the ion implantation process. At high fluences, we observe an unexpected bimodal depth profile and particle size distribution that has not been reported before in DLC. We propose a model that explains this unique distribution of Co atoms using ion collision effects, taking into account the generation of defects, diffusion processes, nanoprecipitate formation, and elemental redistribution in the DLC matrix. These results are significant not only to magnetic semiconductor research but also to all industries that utilise ion implantation techniques. This is because the current models of ion implantation only explain ion distributions in Gaussian or near-Gaussian shapes.[21]

DLC films were synthesised by mass selective ion deposition using butane as the precursor gas. 5 keV $C_3H_6^+$ ions were implanted at a fluence of typically 5×10^{17} molecules cm^{-2}, which results in a thickness of about 100 nm. The use of 5 keV energy allows a greater penetration range, enhancing adhesion through ion beam mixing at the interface. Each molecule upon impact splits into individual atoms with energy distributed based on their mass fraction. The film deposition was carried out at a high vacuum pressure of $\sim 1 \times 10^{-6}$ hPa. This technique allows the selection of specific ion species based on mass separation through the use of a 45° dipole magnet. Accurate control over synthesis parameters such as energy and mass ensures control over the film properties such as sp^2:sp^3 ratio and hydrogen retention.[14]

The films were subsequently implanted with 30 keV Co^+ ions.[22] An ion current density of $\sim 5\,\mu A\ cm^{-2}$ was used avoiding the bulk heating effects from the ion beam. Cobalt is a preferred magnetic ion dopant as it is known to be incorporated in the diamond lattice[23] and semiconductor materials[24] and is believed to lead to a dilute magnetic semiconductor.[23,24] The Co implantation was carried out at a high vacuum pressure of $\sim 1 \times 10^{-7}$ hPa. In this letter, we present results from DLC films implanted with Co fluences, F, ranging from $F = 1.2$ to $7 \times 10^{16}\,cm^{-2}$ that are sufficient to depict the evolution of the Co depth profile from a unimodal to bimodal distribution. It was observed that fluences larger than $F = 7 \times 10^{16}\,cm^{-2}$ start showing significant losses of Co due to sputtering of already implanted atoms.

High resolution Rutherford backscattering spectrometry (HRBS) was used to measure the distribution of cobalt in the implanted DLC films. A 500 keV $^4He^+$ beam was used to measure the Co depth profiles with a depth resolution of 1.1 nm at the surface. The incident beam hit at an angle of 53° to the sample surface and scattered particles was measured at an angle of 65°. The scattered beam was energy resolved by a 90° dipole magnet and detected by using a position sensitive multi-channel plate detector.[25] The spectra were fitted with SIMNRA software[26,27] to extract the depth profile of Co as shown in Figure 1.

In Figure 1, the abscissa represents the energy of the backscattered He^+ particles and the ordinate represents the backscattering yield. At a fluence of $F = 1.2 \times 10^{16}\,cm^{-2}$, the cobalt atoms assume a Gaussian depth distribution with the maximum cobalt concentration at the projected range, Rp. As the fluence is increased to $F = 2.4 \times 10^{16}\,cm^{-2}$, the measured Co distribution changes from a unimodal to a bimodal distribution. Of the two peaks observed, one is

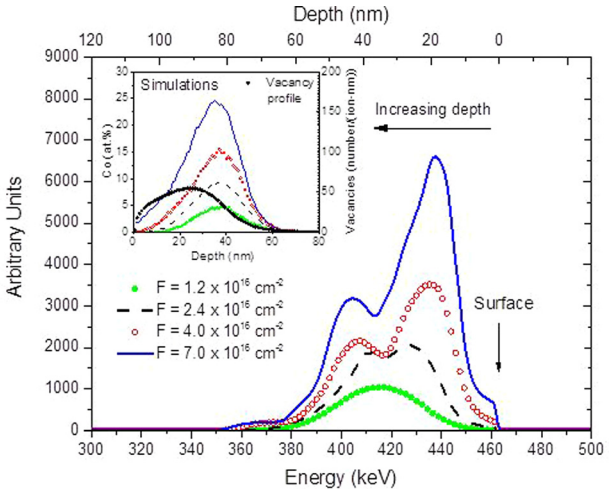

FIG. 1. Co depth profile from SIMNRA analysis of HRBS measurements of Co implanted samples. The inset shows Co depth profiles obtained from D-TRIM simulations for 30 keV implantation of Co into DLC. A constant density of 1.51 g cm^{-3} was used to calculate the depth profile from the RBS data and also used to compute the D-TRIM simulations. A representative vacancy profile is also shown for a fluence of $2.4 \times 10^{16}\,cm^{-2}$.

located closer to the surface and before Rp and the other further from the surface and beyond the Rp. The peak near the surface will, from here onwards, be referred to as the "surface peak" and the peak further from Rp and the surface as "interface peak". It can be seen that the surface peak has a higher yield and a greater lateral spread than the interface peak. The arrow in Figure 1 indicates the energy of ions scattered from Co at the sample surface; clearly, a minor percentage of the Co does reach the surface of the DLC layer. As we increase the fluence to $4 \times 10^{16}\,cm^{-2}$, the bimodal distribution becomes more distinct. The distance of the surface and interface peak from Rp increases, and there is a greater concentration of Co atoms at the surface. The most significant feature is that the surface peak now accumulates nearly twice the amount of cobalt as the interface peak. This trend continues as we increase the fluence. At $F = 7 \times 10^{16}\,cm^{-2}$, both the surface and interface peaks move further away from Rp. There is a greater cobalt accumulation at the surface and in the surface peak.

Typically, ion implantation processes can be simulated, with near quantitative accuracy, by Monte Carlo simulation programmes; therefore the Dynamic TRIM code[28] was used to simulate the profile of implanted cobalt atoms in DLC. In the simulation, an ion energy of 30 keV, a DLC density of 1.51 g cm^{-3}, and an initial composition of 75 at. % carbon and 25 at. % hydrogen based on resonant nuclear reaction measurements (RNRA) were used.[29] The density and composition were obtained from RBS, RNRA, and TEM results. For monoenergetic Co ion implantation in a DLC matrix, Dynamic TRIM predicts the implantation profiles shown in the inset of Figure 1; essentially, Gaussian distributions with a projected range of 35–38 nm accompanied by the straggling of 8 nm. The predicted vacancy profile is also shown where the vacancy peak is located in the near surface region before the projected range.

The experimental results agree with the simulations at low fluence but clearly not at higher fluences. As the fluence increases from 1.2 to $2.4 \times 10^{16}\,cm^{-2}$, the distribution

becomes bimodal and the surface and interface peaks appear. There is neither a theoretical basis nor experimental evidence to suggest dual projected ranges for a mono-energetic ion implantation into any material. Therefore, it is concluded that the implanted atoms still accumulate at the projected range but rearrange in the DLC matrix after reaching Rp due to other processes. The direction of rearrangement suggests that the process is initially driven by the concentration gradient found in the simulated Gaussian profile that involves localised diffusion effects.[30] This surprising bimodal distribution can only be explained by considering different routes through which energy deposited during implantation is dissipated in DLC.

It is to be noted that mono-energetic ion implantations in general lead to a depth distribution of dopants with concentration gradients. However, along with the concentration gradient, an activation energy is required for the implanted atoms to diffuse. Hydrogenated DLC is an excellent thermal insulator ($0.3\,W\,mK^{-1}$).[31] Thus, unlike other materials, it takes longer for energy release during thermal spikes to be dissipated as heat.[32] This prolonged exposure to 'heat' released during relaxation of thermal spikes enhances localised diffusion of the Co atoms. This model is supported by a previous report of a bimodal distribution observed in silica, which is another good thermal insulator.[33] This also explains why similar bimodal distributions are not observed in other materials such as silicon at room temperature implantation.[34]

Another primary effect of ion implantation that becomes increasingly significant with higher fluences is defect generation. In hydrogenated DLC, the defects are primarily in the form of hydrogen vacancies that can result in effusion and massive redistribution of hydrogen.[16,29,35] This can lead to porous channels within the DLC matrix aiding inter-atomic diffusion. The vacancy peak is located in the near-surface region before the projected range. This explains why the diffusion length of Co atoms towards the surface is significantly longer than that towards the interface. Other major effects are rehybridisation of carbon atoms from sp^3 to sp^2 bonding and clustering of sp^2 carbon atoms within DLC films.[16] These regions can act as traps and diffusion sinks for the Co atoms.

TEM lamellae preparation was done by *in situ* lift-out using a Zeiss Crossbeam NVision 40 system. After protecting the surface of the DLC films with a platinum cap layer, each TEM lamella was prepared using a 30 keV Ga FIB with adapted currents. Transfer to a 3-post copper lift-out grid (Omniprobe) was done with a Kleindiek micromanipulator. To minimize the sidewall damage, Ga ions with a terminal energy of only 5 keV were used for final thinning of each lamella. TEM investigations were carried out using an image C_s-corrected Titan 80–300 microscope (FEI) operated at an accelerating voltage of 300 kV. Besides bright-field TEM (BF-TEM) images, high-resolution TEM (HR-TEM) micrographs were taken to characterize the microstructure of the DLC films. Prior to each TEM analysis, the specimen mounted in a double-tilt analytical holder was placed for 10 s into a Model 1020 Plasma Cleaner (Fischione).

Figure 2 shows cross-sectional BF-TEM images of the Co-implanted DLC films. Nanoparticles are observed in all the implanted films. When the concentration of a dopant, in this case cobalt, exceeds the solubility limit of the matrix, it becomes energetically favourable for the dopants to cluster into nanoparticles.[36–38] The driving mechanism behind this phenomenon is the reduction in surface energy of the dopant atoms in the form of nanoparticles as compared to free atoms and chemical interactions with the base matrix.[36]

For the sample implanted with $F = 1.2 \times 10^{16}\,cm^{-2}$, some implanted atoms cluster into nanoparticles characterized by a mean diameter of 1.2 ± 0.5 nm. As the fluence increases, the particle size also increases. For $F = 2.4 \times 10^{16}\,cm^{-2}$, it is 1.5 ± 0.7 nm. Since the nanoparticles closer to the surface are slightly larger than those seen in larger depth, the error in the mean particle diameter, which is given as two times of the standard deviation, is slightly larger for $F = 2.4 \times 10^{16}\,cm^{-2}$. Also, the region in which the nanoparticles are spread increases slightly. The bimodal distribution observed in the RBS spectra is, however, only distinctly visible for the sample implanted with $F = 7 \times 10^{16}\,cm^{-2}$. A dense region near the surface is observed that is accumulated with nanoparticles with a size of 2.9 ± 1.9 nm. This region represents the surface peak, and it coincides with the vacancy peak observed in the simulated vacancy profile. This shows that the defects generated during implantation act as nucleating sites for the nanoparticle formation and their subsequent growth. This is followed by a region with a decreased density of nanoparticles. This depletion region in turn is followed by the interface peak with a higher density of nanoparticles characterized by a mean diameter of 1.6 ± 0.7 nm. The previous report of ferromagnetic order

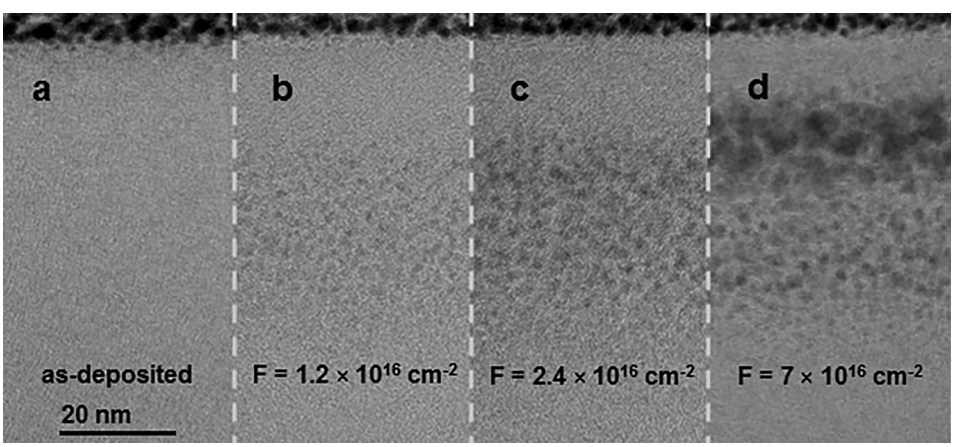

FIG. 2. Cross-sectional BF-TEM images of an as-deposited DLC film (a) and DLC layers Co-implanted with various fluences: (b) $F = 1.2 \times 10^{16}\,cm^{-2}$, (c) $F = 2.4 \times 10^{16}\,cm^{-2}$, and (d) $F = 7 \times 10^{16}\,cm^{-2}$.

in similar Co implanted DLC[20] is likely to be due to the nanoparticles observed in this study.

The cross-sectional TEM images correspond well with the RBS profile. It is to be noted that while RBS spectra show Co atoms reaching the surface layer, there are no nanoparticles seen in the first few nanometres of implanted DLC. Although very small nanoparticles in the order of < 1 nm might be not visible within DLC due to a decreased signal-to-noise ratio, a significant percentage of implanted Co seems to be diluted within the DLC matrix.

The large nanoparticles and the high concentration of Co at the surface peak that is evident at high fluences can be explained by considering the HR-RBS data, D-TRIM simulations, and TEM images. HR-RBS data show that at low fluences, Co follows a Gaussian distribution, but at high fluences, the Co atoms diffuse from the projected range towards the surface and interface. The diffusion of Co atoms towards the surface is higher than that towards the interface due to defect assisted diffusion. This is evidenced by the location of the vacancy peak in the near surface region before the projected range as predicted by D-TRIM simulations. The Co atoms that diffuse towards the surface get trapped in the defects, leading to formation and growth of large nanoparticles as shown in the TEM images. Cobalt atoms located in nanoparticles are immobile and do not further participate in the diffusion process. This ultimately reduces the number of Co atoms diffusing from the surface towards the projected range, thereby leading to the observed Co accumulation at the near surface region. As the fluence increases, the defect concentration increases, leading to larger nanoparticles which lead to further accumulation of Co at the surface peak, thus explaining the bimodal distribution.

Figure 3 shows a representative HR-TEM image of the nanoparticle region of the DLC film Co-implanted with $F = 7 \times 10^{16}\,cm^{-2}$ together with the corresponding Fast Fourier Transform in the inset. Here, diffraction rings are observed pointing to the crystalline nature of the nanoparticles. In particular, distinct d-spacings of 0.248, 0.208, 0.157, and 0.145 nm are determined. They do not coincide with those of metallic cobalt in the cubic or hexagonal phases that occur in the bulk, even assuming a slight variation of the lattice parameters caused by local stress. Co hydrides, such as $CoH_{0.19}$, $CoH_{0.26}$, or $CoH_{0.}34$,[39] can also be excluded. Furthermore, Co carbides, such as Co_2C[40,41] or Co_3C,[41,42] are also unlikely since a higher number of diffraction rings should be visible in the diffractogram. Thus, while crystalline nanoparticles containing Co are observed, the exact phase and composition cannot be determined.

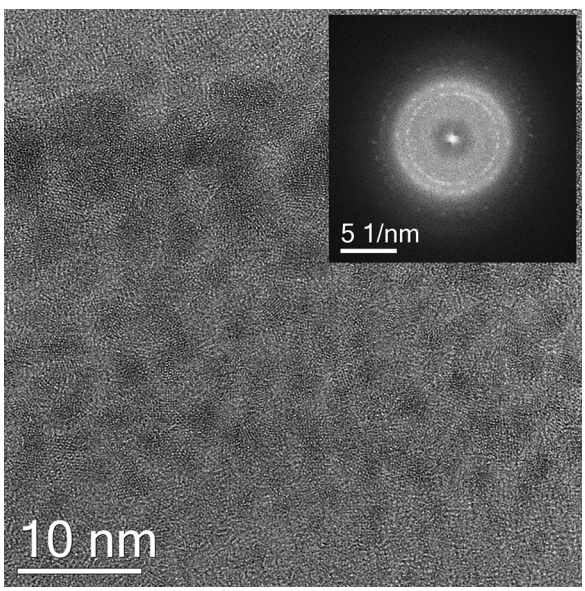

FIG. 3. HR-TEM image of nanoparticles seen in DLC implanted with a Co fluence of $F = 7 \times 10^{16}\,cm^{-2}$. The inset shows the Fast Fourier Transform of the HR-TEM image. Distinctive diffraction rings corresponding to d-spacings of 0.248, 0.208, 0.157, and 0.145 nm point to the presence of crystalline nanoparticles.

Cobalt implantation into hydrogenated DLC results in a bimodal distribution of the implanted atoms. The bimodal distribution along with the nanoparticle formation is explained by diffusion processes enhanced by energy deposited during collision cascades, relaxation of thermal spikes, and defects formed during ion implantation. We also report and explain the formation of nanoparticles, which proves that the Co atoms chemically interact with the DLC matrix, which is crucial for magnetic semiconductors. A bimodal nanoparticle distribution can also lead to interesting magneto-transport properties that are not seen in unimodal distributions. This includes anisotropic magnetoresistances when the current is in-plane or out-of-plane, and the electrical transport is either through both the small and large nanoparticle distributions or first through the small and then large nanoparticle distribution. This may be useful, for example, for anisotropic magnetic sensors. Thus, our research can aid significantly in developing carbon based electronics. Further research in this field can also provide an alternative to thermal annealing, to cause dopant activation and to control the distribution of the implanted atoms in the base matrix in the nanometre regime. Our future work will be towards assessing the magnetotransport and examining the effects of variation in ion species in ion implanted DLC films.

The authors thank A. Kunz for TEM lamellae preparation. Support by the Structural Characterization Facilities Rossendorf at the HZDR Ion Beam Centre is gratefully acknowledged. PhD scholarship and principal investigator funding from the MacDiarmid Institute of Advanced Materials and Nanotechnology, Wellington, New Zealand, is greatly acknowledged.

[1]R. K. Kawakami, E. Johnston-Halperin, L. F. Chen, M. Hanson, N. Guébels, J. S. Speck, A. C. Gossard, and D. D. Awschalom, Appl. Phys. Lett. **77**(15), 2379–2381 (2000).
[2]J. Kennedy, G. V. M. Williams, P. P. Murmu, and B. J. Ruck, Phys. Rev. B **88**(21), 214423 (2013).
[3]Y. Matsumoto, M. Murakami, T. Shono, T. Hasegawa, T. Fukumura, M. Kawasaki, P. Ahmet, T. Chikyow, S.-Y. Koshihara, and H. Koinuma, Science **291**(5505), 854 (2001).
[4]A. Numan, N. Alexei, Z. Hartmut, W. Kurt, B. Hans-Werner, S. Christoph, G. Şafak, B. Asif, K. Rustam, and T. Lenar, J. Phys. D: Appl. Phys. **42**(11), 115005 (2009).
[5]Z. Jia, R. Zhang, Q. Han, Q. Yan, R. Zhu, D. Yu, and X. Wu, Appl. Phys. Lett. **105**(14), 143103 (2014).
[6]A. Wójcik, K. Kopalko, M. Godlewski, E. Guziewicz, R. Jakieła, R. Minikayev, and W. Paszkowicz, Appl. Phys. Lett. **89**(5), 051907 (2006).
[7]J. J. Liu, M. H. Yu, and W. L. Zhou, J. Appl. Phys. **99**(8), 08M119 (2006).
[8]Y. Fukuma, H. Asada, S. Senba, and T. Koyanagi, Appl. Phys. Lett. **108**(22), 222403 (2016).

[9]D. Xu, P. Li, Y. Zhang, Y. Lou, and Y. Li, Thin Solid Films **616**, 573–578 (2016).
[10]J. Kennedy, J. Leveneur, G. Williams, D. Mitchell, and A. Markwitz, Nanotechnology **22**, 115602 (2011).
[11]J. Leveneur, J. Kennedy, G. Williams, J. Metson, and A. Markwitz, Appl. Phys. Lett. **98**(5), 053111–053113 (2011).
[12]T. Prakash, G. V. M. Williams, J. Kennedy, and S. Rubanov, J. Alloys Compd. **667**, 255–261 (2016).
[13]A. Markwitz, B. Mohr, D. F. Carpeno, and R. Hubner, Surf. Coat. Technol. **258**, 956–962 (2014).
[14]A. Markwitz, B. Mohr, and J. Leveneur, Nucl. Instrum. Methods Phys. Res., Sect. B **331**, 144–148 (2014).
[15]K. Suschke, R. Hubner, P. P. Murmu, P. Gupta, J. Futter, and A. Markwitz, Coatings **5**(3), 326–337 (2015).
[16]A. Markwitz, J. Leveneur, P. Gupta, K. Suschke, J. Futter, and M. Rondeau, J. Nanomater. **2015**, 706417 (2015).
[17]J. A. C. Santana, V. Singh, V. Palshin, E. Handberg, A. Petukhov, Y. Losovyj, A. Sokolov, and I. Ketsman, Appl. Phys. A **98**(4), 811–819 (2010).
[18]J. A. C. Santana, R. Skomski, V. Singh, V. Palshin, A. Petukhov, Y. B. Losovyj, A. Sokolov, P. A. Dowben, and I. Ketsman, J. Appl. Phys. **105**(7), 07A930 (2009).
[19]R. Paul, M. K. Sharma, R. Chatterjee, S. Hussain, R. Bhar, and A. K. Pal, Appl. Surf. Sci. **258**(15), 5850–5857 (2012).
[20]P. Gupta, G. Williams, and A. Markwitz, J. Phys. D: Appl. Phys. **49**(5), 055002 (2016).
[21]J. F. Ziegler, M. D. Ziegler, and J. P. Biersack, Nucl. Instrum. Methods Phys. Res., Sect. B **268**(11–12), 1818–1823 (2010).
[22]A. Markwitz and J. Kennedy, Int. J. Nanotechnol. **6**(3–4), 369–383 (2009).
[23]S. R. Shinde, S. B. Ogale, J. S. Higgins, H. Zheng, A. J. Millis, V. N. Kulkarni, R. Ramesh, R. L. Greene, and T. Venkatesan, Phys. Rev. Lett. **92**(16), 166601 (2004).
[24]K. Siraj, M. Khaleeq-ur-Rahman, M. S. Rafique, M. Z. Munawar, S. Naseem, and S. Riaz, Appl. Surf. Sci. **257**(15), 6445–6450 (2011).
[25]T. Osipowicz, H. L. Seng, T. K. Chan, and B. Ho, Nucl. Instrum. Methods Phys. Res., Sect. B **249**(1–2), 915–917 (2006).
[26]M. Mayer, AIP Conf. Proc. **475**(1), 541–544 (1999).
[27]M. Mayer, Nucl. Instrum. Methods Phys. Res., Sect. B **332**, 176–180 (2014).
[28]J. P. Biersack and L. G. Haggmark, Nucl. Instrum. Methods **174**(1), 257–269 (1980).
[29]P. Gupta, H. W. Becker, G. V. M. Williams, R. Hübner, K. H. Heinig, and A. Markwitz, Nucl. Instrum. Methods Phys. Res., Sect. B **394**, 6–11 (2017).
[30]A. Paul, T. Laurila, V. Vuorinen, and S. V. Divinski, *Thermodynamics, Diffusion and the Kirkendall Effect in Solids* (Springer International Publishing, Cham, 2014), pp. 115–139.
[31]M. Shamsa, W. Liu, A. Balandin, C. Casiraghi, W. Milne, and A. Ferrari, Appl. Phys. Lett. **89**(16), 161921–161921 (2006).
[32]G. H. Vineyard, Radiat. Eff. **29**(4), 245–248 (1976).
[33]M. Dubiel, H. Hofmeister, E. Schurig, E. Wendler, and W. Wesch, Nucl. Instrum. Methods Phys. Res., Sect. B **166**, 871–876 (2000).
[34]A. H. van Ommen, J. J. M. Ottenheim, A. M. L. Theunissen, and A. G. Mouwen, Appl. Phys. Lett. **53**(8), 669–671 (1988).
[35]A. Markwitz, P. Gupta, B. Mohr, R. Hubner, J. Leveneur, A. Zondervan, and H. W. Becker, Nucl. Instrum. Methods Phys. Res., Sect. B **371**, 230–234 (2016).
[36]A. L. Stepanov, D. E. Hole, and P. D. Townsend, J. Non-Cryst. Solids **260**(1–2), 65–74 (1999).
[37]H. Hideo, Jpn. J. Appl. Phys., Part 1 **32**(9A), 3892 (1993).
[38]N. Matsunami and H. Hosono, Appl. Phys. Lett. **63**(15), 2050 (1993).
[39]V. K. Fedotov, V. E. Antonov, T. E. Antonova, E. L. Bokhenkov, B. Dorner, G. Grosse, and F. E. Wagner, J. Alloys Compd. **291**(1–2), 1–7 (1999).
[40]J. Clarke and K. Jack, Chem. Ind. **46**, 1004–1005 (1951).
[41]S. Nagakura, J. Phys. Soc. Jpn. **16**(6), 1213–1219 (1961).
[42]L. Y. Markovsky, E. Bezruk, and G. Berlova, Izv. Akad. Nauk SSSR, Neorg. Mater. **7**(1), 56–58 (1971).